https://doi.org/10.1038/s44306-024-00049-w

Current-driven dynamics of antiferromagnetic skyrmions: from skyrmion Hall effects to hybrid inter-skyrmion scattering

Amal Aldarawsheh[1,2] ✉, Moritz Sallermann[1,3,4], Muayad Abusaa[5] & Samir Lounis[1,2] ✉

Antiferromagnetic (AFM) skyrmions have emerged as a highly promising avenue in the realm of spintronics, particularly for the development of advanced racetrack memory devices. A distinguishing feature of AFM skyrmions is the cancellation of their net topological charge, leading to an anticipated absence of the skyrmion Hall effect (SkHE). Here, we unveil that the latter is finite under the influence of spin-transfer torque, depending on the direction of the injected current impinging on intrinsic AFM skyrmions emerging in Cr/Pd/Fe trilayer on Ir(111) surface. Hinging on first principles combined with atomistic spin dynamics simulations, we identify the origin of the SkHE, which is due to the ellipticity of the skyrmions, and we uncover that FM skyrmions in the underlying Fe layer act as effective traps for AFM skyrmions, confining them and affecting their velocity. These findings hold significant promise for spintronic applications, the design of multi-purpose skyrmion tracks while advancing our understanding of AFM–FM skyrmion interactions and hybrid soliton dynamics in heterostructures.

Topologically protected magnetic textures, such as magnetic skyrmions[1–10], have emerged as a subject of immense interest due to their potential to become non-volatile information carriers in future spintronic devices[11–14]. The discovery of magnetic skyrmions in numerous materials, hosting bulk or interfacial Dzyaloshinskii–Moriya interaction (DMI), has spurred extensive research to explore their unique properties and applications[3–6]. Particularly, the concept of skyrmion-based racetrack memory[2,3,15,16] has garnered considerable attention, where skyrmions are dynamically driven by numerous means. These skyrmions possess several advantages, including nanoscale size, significant stability enhanced by their topological nature[1,3,17], the ability to overcome pinning sites[18–23], and a low depinning current (compared to domain walls[24–27]).

Various methods have been proposed to drive magnetic skyrmions, encompassing electric currents[2,15,16,28], spin waves[29], magnetic field gradients [30], temperature gradients[31], voltage-controlled magnetic anisotropy[32–35], and surface acoustic waves[36]. However, one significant challenge that arises during their manipulation, via electrical means or magnetic field gradient[37], is the skyrmion Hall effect (SkHE), wherein skyrmion trajectories deviate from the driving current direction due to the Magnus force[38–40], which is proportional to the topological charge[3]. This undesired effect hampers the precise control and movement of skyrmions in spintronic devices.

In contrast, antiferromagnetic (AFM) skyrmions are expected to be unaffected to the SkHE since the building-block skyrmions carry opposite topological charge, which enforces the motion along the direction imposed by the applied current, due to the cancellation of the Magnus forces predicted theoretically[41–43] and observed for significant distances experimentally[44]. Moreover, AFM skyrmions are in general insensitive to external magnetic fields[45–50], which overall aids their discovery and control for promising implementation in devices. Following extensive phenomenology-based predictions[41,43,47,51–54], FM skyrmions coupled antiferromagnetically through a spacer, so-called synthetic AFM skyrmions, were realized in multilayers[44,55–59], while complex AFM topological objects were identified in bulk materials[60–62]. Ab initio simulations predicted the emergence of intrinsic AFM skyrmions in Cr films and frustrated multimeronic states in Mn films interfaced with Ir(111) surface[49,63]. In this context, intrinsic means that the AFM solitons are hosted within the same AFM material.

Here, we explore the dynamical response of intrinsic AFM skyrmions to an applied current. We consider the scenario of a magnetic tunnel

[1]Peter Grünberg Institute, Forschungszentrum Jülich and JARA, 52425 Jülich, Germany. [2]Faculty of Physics, University of Duisburg-Essen and CENIDE, 47053 Duisburg, Germany. [3]RWTH Aachen University, 52056 Aachen, Germany. [4]Science Institute and Faculty of Physical Sciences, University of Iceland, 107 Reykjavík, Iceland. [5]Department of Physics, Arab American University, Jenin, Palestine. ✉e-mail: a.aldarawsheh@fz-juelich.de; s.lounis@fz-juelich.de

junction (MTJ), where a magnetic electrode injects a perpendicular-to-plane spin-polarized current (SP-CPP) with in-plane polarization on Cr/Pd/Fe thin films deposited on Ir(111) surface predicted from first principles to host intrinsic AFM skyrmions[49] (Fig. 1). Counter-intuitively, we demonstrate that these skyrmions exhibit a significant SkHE, which is strongly anisotropic, i.e., that is dependent on the polarization direction of the applied spin current. We identify the origin of the SkHE and its vanishing conditions, which permits the design of a track either with, or without, the SkHE. We unveil complex interactions between intrinsic AFM skyrmions, hosted in Cr, and various spin textures, including individual FM skyrmions, found in Fe. This unique hybrid scenario enables the exploration of AFM–FM inter-skyrmion dynamics. The mutual inter-skyrmion interactions lead to a non-trivial two-dimensional energetical map, with pinning and repulsive centers. These impact both the trajectory and velocity of AFM skyrmions and provide pinning and deflection processes. Our findings pave the way for further exploration and control of skyrmion-based devices and applications in antiferromagnetic storage systems.

Results

Trajectories of AFM skyrmions driven by perpendicular-to-plane currents

We investigate current-induced dynamics of single and interchained AFM skyrmions (Fig. 1f, g), emerging at the Cr layer when deposited on Pd/Fe/Ir(111) with fcc stacking (Fig. 1e). Pd/Fe/Ir(111) is a well established thin film material that hosts spin spirals, which can be deformed into FM skyrmions upon application of a magnetic field[18,21,64–70]. Once covered with a Cr layer, a row-wise AFM (RW-AFM) state emerges, which hosts individual or catenated AFM skyrmions[49] even without applying an external magnetic field. RW-AFM states, in a triangular lattice, are not common in nature[71,72] and arise due to the interplay of the neighboring Heisenberg exchange interactions (J)[50,73]. The presence of both the DMI and an out-of-plane magnetic anisotropy (K) stabilizes the highly sought intrinsic AFM skyrmions. Due to the magnetic interactions among Cr atoms, calculated from ab initio (see "Methods") and depicted in Supplementary Fig. 1, the spins in the Cr layer are distributed among four sublattices (L1–L4). Ferromagnetically aligned spins on one sublattice host a single FM skyrmion, which is coupled to FM skyrmions, emerging in other sublattices, to form AFM skyrmions. Single and interchained AFM skyrmions can form by populating the distinct sublattices in different fashions (Fig. 1f, g). Here we employ atomistic spin dynamics simulations, applying the Landau–Lifshitz–Gilbert (LLG) equation, augmented with spin-transfer torque (STT) terms[41,42,74–76]. As described in the Methods section, we explore the current-driven motion of the AFM skyrmions, by injecting perpendicular-to-plane currents with in-plane polarization (Fig. 1a–d). In this scenario, one expects a straight motion of an AFM skyrmion along the direction perpendicular to the polarization $\mathbf{S}_p$ of the applied spin current j_s[41,42], as illustrated in Fig. 1b–d.

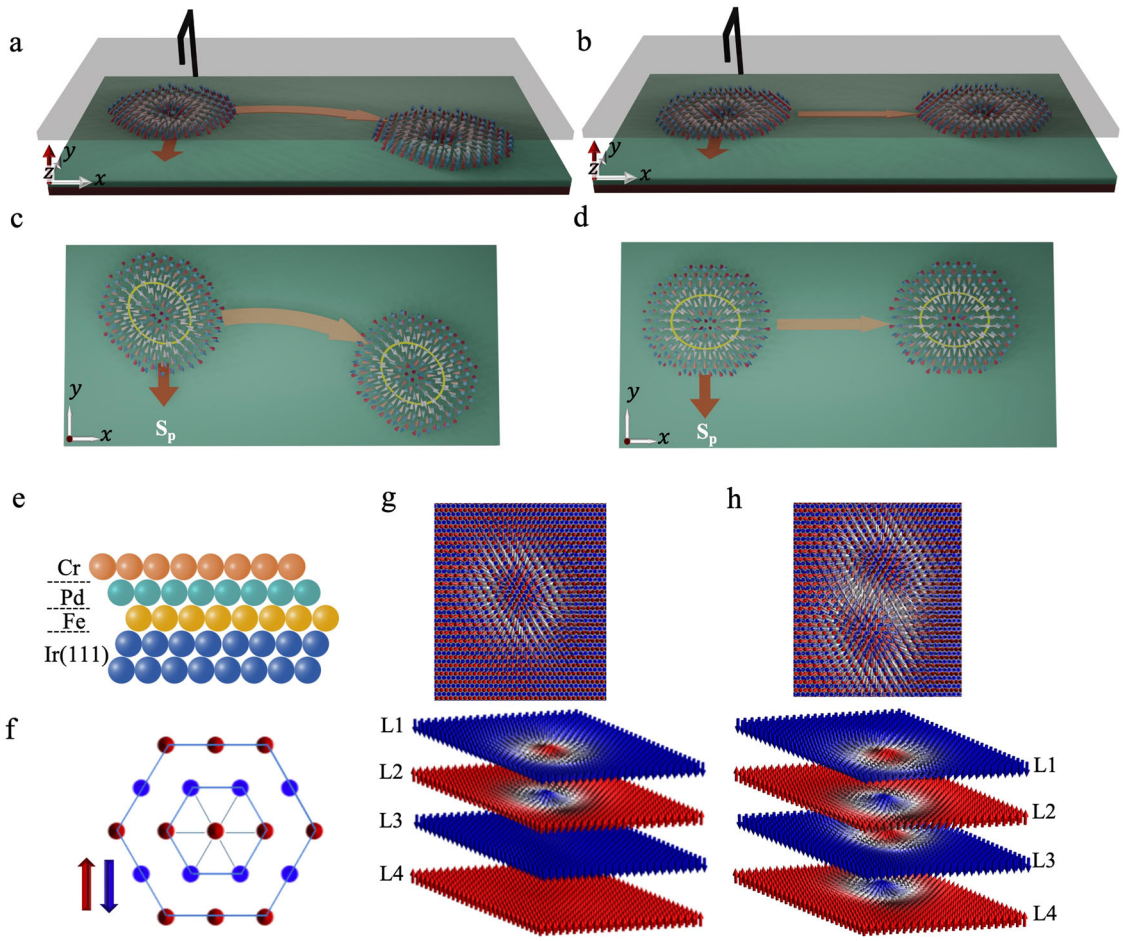

Fig. 1 | Current-driven dynamics of AFM skyrmions. a, **b** Schematic representations of CPP-induced motion of an elliptical AFM skyrmion showing the SkHE (**a**) or not (**b**) depending on the alignment of the polarization of the applied current $\mathbf{S}_P$ with respect to the skyrmion. **c**, **d** Top view of (**a**, **b**), respectively. **e** Schematic representation of the material hosting intrinsic AFM skyrmions at the triangular lattice of a Cr layer grown on Pd/Fe film deposited on an fcc(111) surface of Ir. **f** The ground state in the Cr layer is the row-wise AFM configuration illustrated in the top view of the surface as red and blue spheres for different orientation of the spins. Snapshots of single (**g**) and double (**h**) overlapping AFM skyrmions emerging in the Cr film with the spins distribution among four sublattices L1–L4. See also ref. 49.

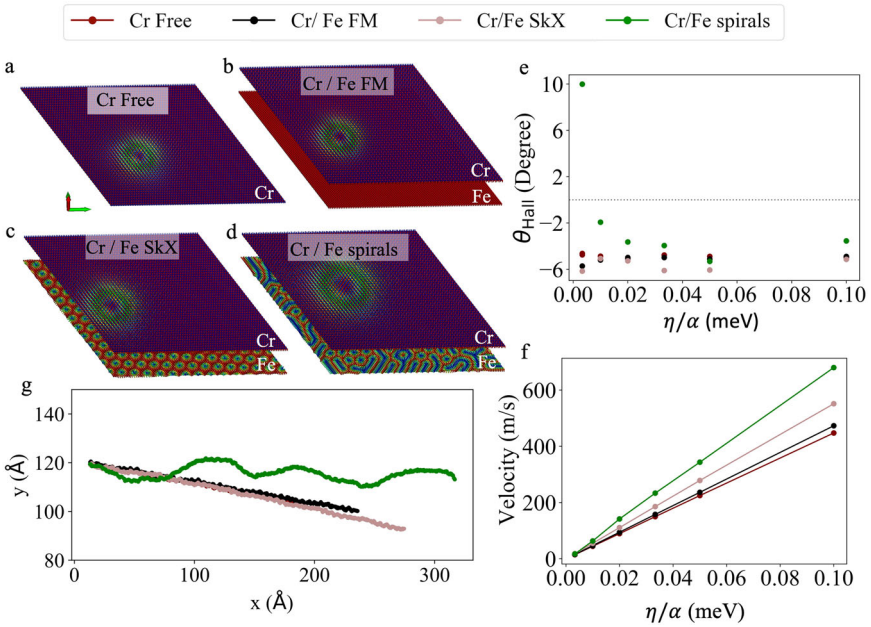

Fig. 2 | Transitional motion of elliptical AFM skyrmion driven by SP-CPP currents. **a**–**d** Snapshots of the AFM skyrmion at Cr layer in four different cases: **a** Cr freestanding case, where the magnetic interactions with Fe layer are not included (AFM skyrmion radius is 2 nm); **b** Fe interactions are included with a finite magnetic field saturating Fe into a FM state (AFM skyrmion radius is 2.1 nm), while **c** a weaker magnetic field leads to a skyrmion lattice (SkX) which slightly enlarges the AFM skyrmion (radius of 2.5 nm); **d** in the absence of a magnetic field spirals emerge at Fe layer (AFM skyrmion reaches a radius of 3.2 nm). **e** Impact of the current parameter ratio η/α on the skyrmion Hall angle, and **f** on velocity. **g** The trajectories of the AFM skyrmion for cases in (**a**–**d**) with $\eta/\alpha = 0.01$ meV.

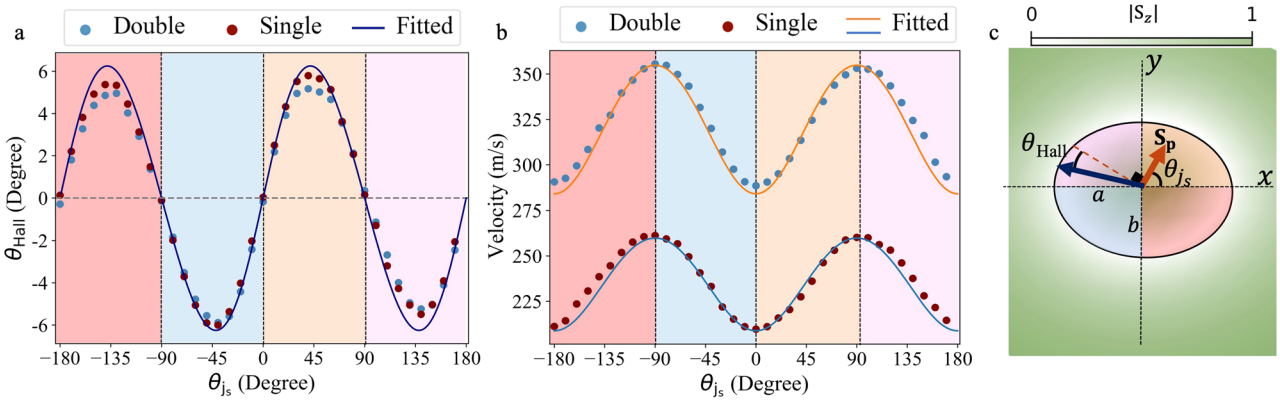

Fig. 3 | Influence of the direction of current polarization on the skyrmion Hall angle and velocity of elliptical AFM skyrmions. For conciseness, we consider here as an example the Cr freestanding layer case. **a** The skyrmion Hall angle and **b** the absolute value of the velocity of AFM skyrmions as a function of the angle θ_{j_s} between the current polarization direction and the major ellipse axis, for single (brown) and double (blue) AFM skyrmions, with $\eta/\alpha = 0.05$ meV. **c** Schematic representation of the AFM skyrmion showing an elliptical shape, with a long (short) axis defining the x axis (y) axis. The angles associated with the spin polarization of the current $\mathbf{S}_\mathrm{p}$ and the SkHE are displayed. The colored regions within the ellipse correspond to those shown in (**a**, **b**).

We initiate our study by investigating the case of single AFM skyrmions (Fig. 1a–d) and consider two possibilities: either (i) by neglecting the Cr–Fe magnetic exchange interactions, which corresponds to a freestanding Cr film (Fig. 2a), or (ii) not by scrutinizing various magnetic states in Pd/Fe, which can be tuned by applying a magnetic field (Fig. 2b–d). For the latter, we consider the case of a saturated FM state in the Fe film (Fig. 2b), which is obtained upon application of a large magnetic field, while a moderate field can transition the spin-spiraling state shown in Fig. 2d to a skyrmion lattice (SkX) illustrated in Fig. 2c[18,66]. The effective impact of the spin current can be monitored via the current parameter η, which is directly proportional to j_s (see "Methods").

As mentioned before, AFM skyrmions exposed to spin-polarized currents via STT, typically do not experience a SkHE[41–44,77] while their velocity is expected to be proportional to η/α in the case of CPP injection[77]. Surprisingly, our AFM skyrmions exhibit an unexpected dynamical behavior, deviating from conventional expectations. Independently from the Cr–Fe interaction and the nature of the magnetic state pertaining to the Pd/Fe film, the Hall angle is, generally, found to be around −5° (negative sign means the deviation is clockwise), which remains consistent across various η/α values (Fig. 2e). Deviations occur, however, for weak driving forces (small η/α) when Cr is placed atop Fe spin spirals. Indeed, the AFM skyrmions display irregular scattered trajectories as depicted in Fig. 2g, due to uncontrolled scattering at various spin textures emerging in Fe. In this particular case, the extraction of the Hall angle is not trivial, since the skyrmion trajectories are not straight. Interestingly, the Fe spirals can deflect the AFM skyrmions strongly, which can lead to effective Hall angles larger than 10°, as calculated up to average distances of about 90 nm.

The velocity of the skyrmions is linear with η/α, with the largest speed found when Fe hosts a spirals state (Fig. 2f). Intriguingly, the Cr–Fe interaction, in general, favors large skyrmion velocities, which can be traced back to the size of the skyrmions. Indeed, the Cr–Fe interaction enlarges the diameter of the AFM skyrmion, which is known to increase its velocity[52,78], as unveiled in the following analysis. Examples of skyrmion trajectories are shown in Supplementary Movies 1–3.

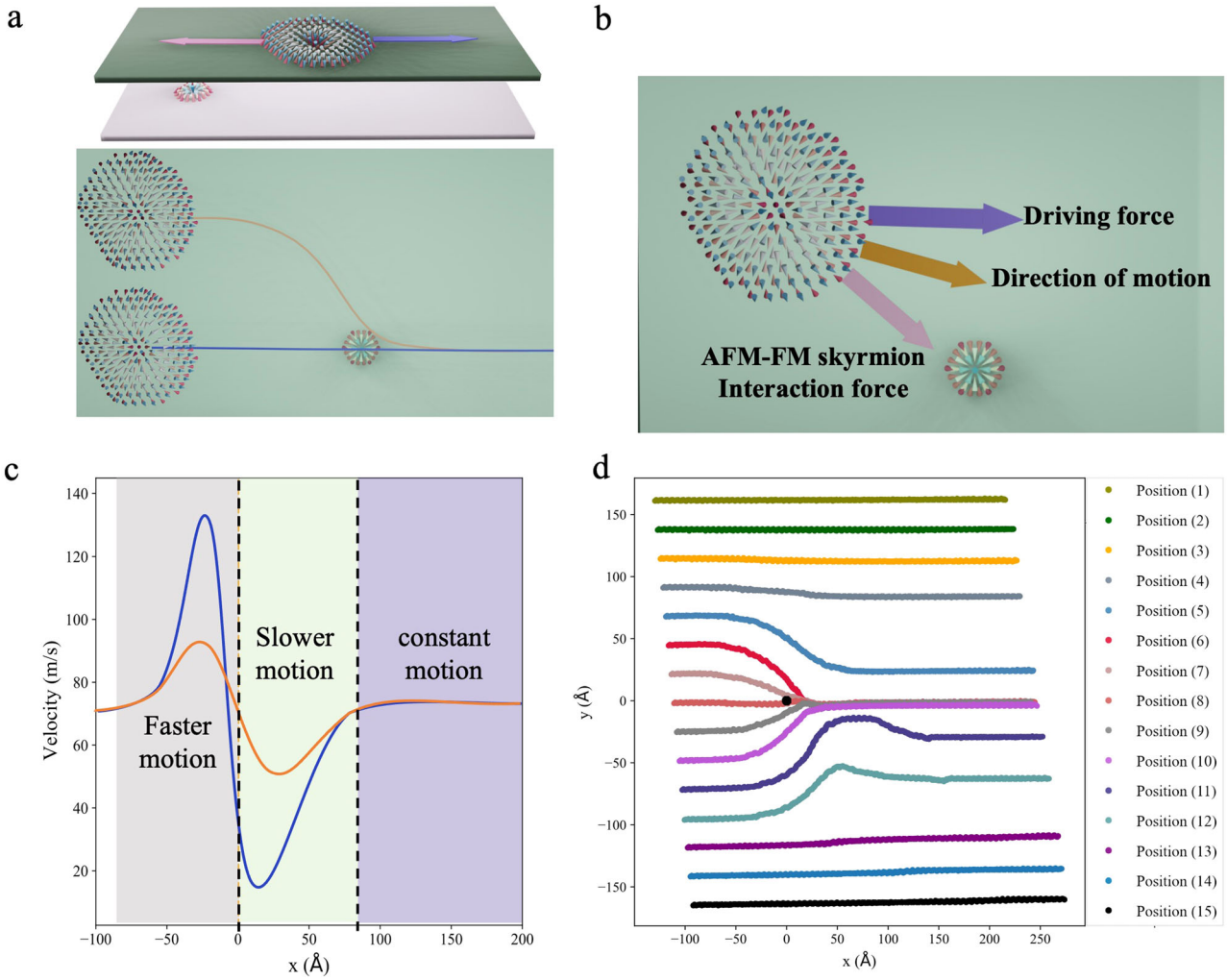

Fig. 4 | Position dependent deflection of AFM skyrmions due to the AFM–FM skyrmionic interaction. a, **b** Schematic representation of the forces acting on the AFM skyrmion: The driving force due to the applied spin current and the AFM–FM skyrmionic interacting induced by the FM skyrmion in the Fe layer through the Pd spacer. **a** Two trajectories with different starting points are illustrated. **c** Schematic representation of the effect of the Fe–FM skyrmion on the velocity of the AFM skyrmion with the blue and orange lines corresponding to the paths shown in (**a**). **d** The trajectory of the AFM skyrmion shown in (**a**) when current-driven toward a pinned FM skyrmion considering different initial positions (motion from left to right). Deflection in the motion direction occurs depending on the relative position between the AFM and FM skyrmions.

Figure 2e, f is just the tip of the iceberg. By analyzing the skyrmion dynamics as a function of the direction of the applied current, we unveil a rich anisotropic response: both the skyrmion Hall angles and velocities are modified and we identify directions along which the SkHE cancels out. Before discussing the anisotropic current-driven dynamical response, we briefly address the origin of this behavior, which is induced by the ellipticity of the AFM skyrmions emerging in Cr/Pd/Fe/Ir(111) surface. By carefully scrutinizing the AFM skyrmions, one can identify an elliptical shape. For instance, the single AFM skyrmion shown in Fig. 3c has a major and minor axis of 2.2, and 1.8 nm, respectively. Upon formation of a double AFM skyrmion, the shape of the skyrmions remains elliptical. The size of the skyrmions forming the solitonic dimer, increases significantly, enlarging both the major and minor axes of the skyrmion building blocks to 3 nm and 2.4 nm, respectively. The origin of the observed ellipticity can be traced back to the anisotropic magnetic environment experienced by the spins residing in the AFM skyrmion due to the interplay between the neighboring exchange interactions in the triangular lattice. The lattice can be decomposed into four sublattices carrying distinct magnetic states (a more detailed analysis is provided in Supplementary Notes 1 and 2 and Supplementary Fig. 2). Phenomenologically, one can demonstrate that by tuning the underlying interactions, the skyrmions can be reshaped into an isotropic form[50]. We note that this is clearly a material dependent property.

Directionality of the current-driven elliptical AFM skyrmions

To explore the anisotropic current-driven response of the AFM skyrmions, we focus on the case of the freestanding Cr layer, i.e., with the Cr–Fe interaction switched-off. This is also representative of the behavior found when the interaction is switched on, while the Fe film hosts either the skyrmion lattice or the saturated FM state. As an example, we inject a current with $\eta/\alpha = 0.05$ meV, but varying systematically the angle between the in-plane current and the major axis of the ellipse, θ_{j_s}, which is represented by the dashed orange line in Fig. 3c.

The skyrmion Hall angle, as a function of θ_{j_s}, is illustrated in Fig. 3a, which clearly shows an oscillating behavior, for both the single (brown) and double (blue) AFM skyrmions, with color-coded regions corresponding to colored areas depicted in Fig. 3c. Figure 3a shows that θ_{Hall} is suppressed when the current is polarized along the two ellipse axes. It reaches the maximum value of about 6° when $\theta_{j_s} = 42°$. Notably, it is not only the Hall angle that changes with θ_{j_s}; the absolute value of the velocity of AFM skyrmions also varies as shown in Fig. 3b, exhibiting the maximum

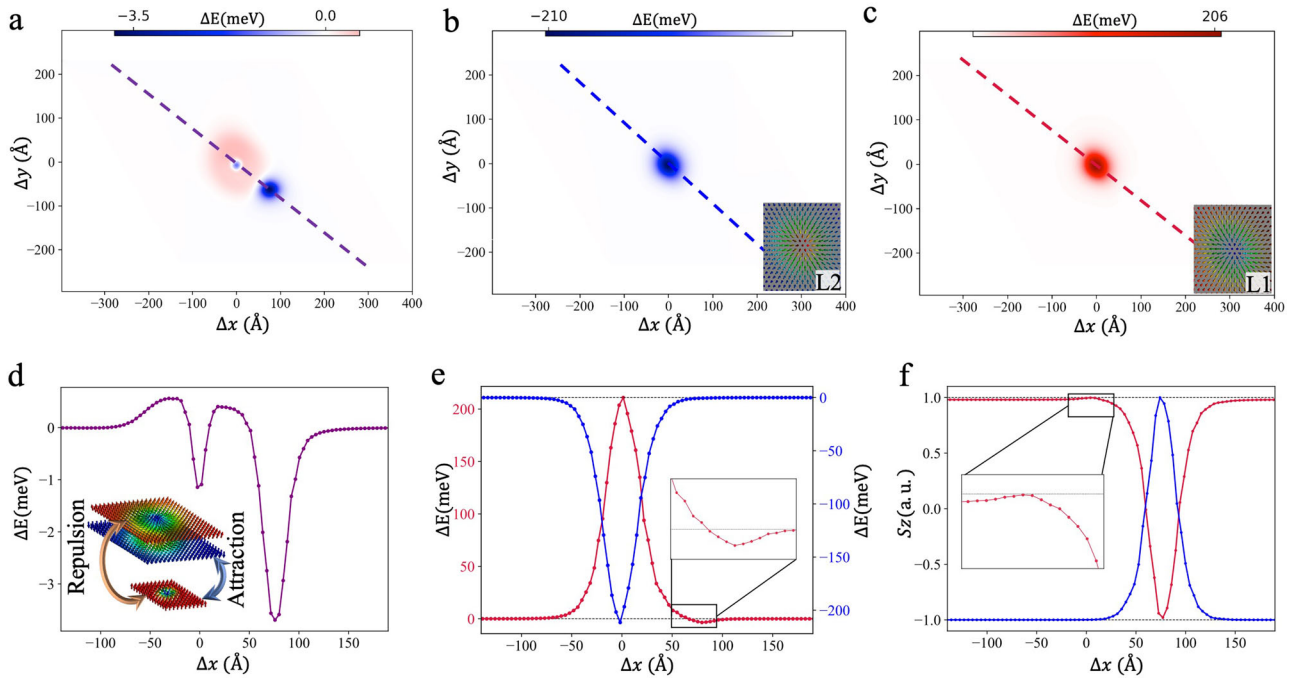

Fig. 5 | AFM–FM skyrmion interaction profile. a Two-dimensional heatmap of the total energy difference resulting when rigid-shifting the AFM skyrmion all over the lattice with the presence of Fe–FM skyrmion at the center of the Fe layer. The energy difference is taken with respect to the case when the two skyrmions are not interacting. This energy difference is further decomposed into the interaction with the AFM skyrmions building blocks: the red-cored FM skyrmion residing at sublattice L2 (**b**), which is of an attractive nature, and the interaction with the blue-cored skyrmion residing at sublattice L1 (**c**), which is of repulsive nature. **d** Energy profile along the purple line indicated in (**a**), decomposed in (**e**) into the L2 blue and L1 red contributions. **f** The z component of the spin in the two sublattices L1 (blue) and L2 (red) along the purple line when the AFM skyrmion positioned at the second minimum shown in (**a**). Inset in (**d**) is a schematic representation of the nature of the interaction between the building blocks of the AFM skyrmion and the FM Fe skyrmion.

(minimum) velocity when the skyrmions move along the ellipse major (minor) axis. Interestingly as depicted in Fig. 3a, double and single AFM skyrmions show the same Hall angle when subjected to the same polarized currents. However, the double AFM skyrmion moves faster than the single one (Fig. 3b).

Thiele equation for elliptical AFM skyrmions

To investigate these intriguing findings further, we analyze the Thiele equation[79] governing AFM skyrmions[43,51,80,81] driven by CPP[42,77,82], simplified to the particular system that we are investigating (see more details in Supplementary Note 3):

$$\alpha\mathcal{D}\cdot\mathbf{v}-\mathcal{B}\cdot\mathbf{S}_p=0\,. \tag{1}$$

The gyrovector cancels out and thus does not contribute to the Thiele equation of AFM skyrmions. Moreover, the effective mass emerging for AFM skyrmions is neglected due to the large AFM exchange interaction[51,81] (see Supplementary Note 3). $\mathbf{v}$ denotes the absolute value of the skyrmion velocity while $\mathbf{S}_p=(\cos\theta_{j_s},\sin\theta_{j_s})$ stands for the unit vector defining the spin polarization direction of the injected current. Note that the x and y axes are defined by the semi-major and semi-minor axes of the elliptical skyrmion, respectively (see Fig. 3c). $\mathcal{B}$ is the driving force tensor, and $\mathcal{D}$ is the dissipative tensor for the whole AFM skyrmion. If the skyrmions were isotropic in shape, the velocity would be perpendicular to the polarization of the current, and there would not be a SkHE.

For each building-block FM skyrmion i forming the AFM skyrmion, the associated components of the dissipative tensor[83], (assuming skyrmions of identical size and shape, are given by: $(\mathcal{D}^i_{xx},\mathcal{D}^i_{yy})=\frac{\pi^2}{8}\left(\frac{b}{a},\frac{a}{b}\right)$, where a, and b are the semi-major and semi-minor ellipse axes, while $\mathcal{D}^i_{yx}=\mathcal{D}^i_{xy}=0$. The components of the driving force tensor are $(\mathcal{B}^i_{xy},\mathcal{B}^i_{yx})=\frac{\gamma\pi}{8}\eta(-b,a)$ and $\mathcal{B}^i_{xx}=\mathcal{B}^i_{yy}=0$. The skyrmion velocity is then given by:

$$\mathbf{v}=\frac{1}{\alpha}\left(\frac{\mathcal{B}_{xy}}{\mathcal{D}_{xx}}\sin\theta_{j_s},\frac{\mathcal{B}_{yx}}{\mathcal{D}_{yy}}\cos\theta_{j_s}\right)=\frac{\gamma\eta a}{\pi\alpha}\left(-\sin\theta_{j_s},\frac{b}{a}\cos\theta_{j_s}\right), \tag{2}$$

$$|\mathbf{v}|=\frac{\gamma\eta a}{\pi\alpha}\sqrt{\sin^2\theta_{j_s}+\frac{b^2_{sk}}{a^2_{sk}}\cos^2\theta_{j_s}}\,, \tag{3}$$

where one immediately notices that, if the skyrmions were circular isotropic, the polarization of the spin current would be perpendicular to the velocity since $\mathbf{v}\cdot\mathbf{S}_p=0$. The propagation direction, associated with the isotropic case, defines the reference angle from which the skyrmion Hall angle is measured $\theta_{\rm ref}=\arctan\frac{v_y}{v_x}=\theta_{j_s}+\frac{\pi}{2}$. Therefore, the Hall angle is evaluated from

$$\theta_{\rm Hall}=\arctan\left[\frac{b}{a}\tan\left(\theta_{j_s}+\frac{\pi}{2}\right)\right]-\left(\theta_{j_s}+\frac{\pi}{2}\right). \tag{4}$$

With these findings at hand, we can explain the behavior of the AFM skyrmions. If the current is polarized along the major or minor axes of the spins (i.e., θ_{j_s} is a multiple of $\frac{\pi}{2}$), the Hall angle cancels out, which gives rise to the extrema of the velocity given by $\frac{\gamma\eta b}{\pi\alpha}$ for $\theta_{j_s}=0,\pi$ (minimum) and $\frac{\gamma\eta a}{\pi\alpha}$ for $\theta_{j_s}=\frac{\pi}{2},\frac{3\pi}{2}$ (maximum). The ratio $\frac{b}{a}$, which is about 0.8 for both the single and double AFM skyrmions, influences the magnitude of the Hall angle as well as the range of oscillations in the velocity. This means, with elliptical AFM skyrmions, we have two more degrees of freedom to manipulate the CPP-induced motion of the AFM skyrmions, where the skyrmion exhibits its maximum velocity when injecting currents polarized along its minor axis, resulting in a Hall free motion along the major axis. This analysis goes along with our findings, depicted in Fig. 3b, where the double AFM skyrmion with

dimensions of $(a, b) = (3, 2.4)$ nm moves with maximum velocity of 355 m/s while the single AFM skyrmion with smaller size (dimensions of (2.2, 1.8) nm), and hence slower motion according to Eq. (2), where its maximum velocity reaches 260 m/s. The maximum Hall angle is expected for $\theta_{j_s} + \pi/2 = \arccos\sqrt{\frac{b}{a+b}}$, which leads to $\theta_{j_s} = 42°$ and $\theta_{\text{Hall}} = 6.2°$ in agreement with the numerical findings of the previous section. Notably, the impact of ellipticity on the motion of FM skyrmions subjected to spin currents was discussed in refs. 83–85.

Current-driven dynamics of AFM skyrmions interacting with FM skyrmions

In Fig. 2g, we unveiled that, when the Fe substrate hosts spirals with an inhomogeneous distribution of FM skyrmions, the intrinsic AFM skyrmions, driven in the Cr overlayer, exhibit typical dynamics pertaining to interactions with defects. In this section, we explore the synthetic configuration of an AFM skyrmion, interacting with a FM skyrmion through a Pd film. This scenario is trivially realized in a Cr/Pd/Fe/Ir(111) surface by applying an out-of-plane magnetic field, which reduces the size of the FM skyrmions in Fe and transforms the lattice configuration into individual topological objects. By applying a spin-polarized current, as done previously, we drive an AFM skyrmion, in the Cr film, toward a pinned FM skyrmion, hosted by the Fe layer. We consider two cases, where either the planned skyrmion trajectory passes trough the FM skyrmion, or it is shifted (see Fig. 4a, b).

We notice that with a weak applied current, the AFM skyrmion gets pinned at the FM skyrmion (see example $\eta/\alpha = 0.001$ meV in Supplementary Movie 4), which clearly indicates the attractive nature of the FM-AFM skyrmion interaction. A stronger current, e.g., $\eta/\alpha = 0.017$ meV, enables the AFM skyrmion to escape the trapping FM soliton, following a roller-coaster-like motion, with an absolute value of the velocity increasing from the initial 75 to 130 m/s, which is attained when getting close to the FM skyrmion, leading to a "speeding up zone", as shown in Fig. 4c. Once the AFM skyrmion overtakes the FM skyrmion, the velocity reduces by about 88% down to around 15 m/s, due to the FM-AFM skyrmion interaction that opposes the driving force and leads to a "slowing-down zone". As the AFM skyrmion moves away from the FM skyrmion, only the driving force dictates its motion, resulting in a "constant motion regime", depicted in Fig. 4c and Supplementary Fig. 3, where the velocity stabilizes at ~75 m/s.

If the AFM skyrmion is off-centered, with respect to the FM skyrmion, their mutual attractive interaction is capable of deviating the underlying trajectory, bringing the AFM skyrmion into the vicinity of the FM skyrmion, as depicted schematically in Fig. 4b and demonstrated systematically for different paths illustrated in Fig. 4d and Supplementary Figs. 3–5. Due to the AFM–FM skyrmion attraction, the AFM skyrmion deflects at the vicinity of the FM skyrmion and then continues its motion along a straight line with a velocity of 75 m/s. Intriguingly, a second deflection manifests after passing the FM skyrmion, when the AFM skyrmion starts an approach from positions (11) and (12). This signals a non-trivial energy profile of the hybrid AFM–FM skyrmionic interaction.

AFM–FM skyrmion interaction profile

To elucidate the underlying reason for the unanticipated second deflection mentioned in the previous section, we analyze the AFM–FM skyrmion interaction profile. Since the AFM skyrmion, in the Cr film, is made of two FM skyrmions oppositely oriented with respect to each other, we expect two competing interactions with the FM skyrmion in the Fe layer, as shown in the inset of Fig. 5d. The FM skyrmions, having their cores pointing in the same direction, and residing in the same ferromagnetic background, would repel each other. Conversely, the FM skyrmions having an opposite magnetic alignment would attract each other. This is clearly illustrated in Fig. 5b, and c, respectively, which shows the energy contribution of both types of coupling to the energy profile, that is obtained by rigidly shifting the AFM skyrmion all over the Cr lattice atop the FM skyrmion pinned in the center of the Fe film. The total interaction heatmap, depicted in Fig. 5a, exhibits a minimum when the AFM skyrmion overlaps with the FM skyrmion, signifying their mutual attraction. In addition, another minimum is observed when the AFM skyrmion is positioned in the lower right part of the FM skyrmion, which represents the global minimum in the rigid shift approximation. This second minimum explains the aforementioned second deflection experienced by the AFM skyrmion, as noted in the previous section.

The surprising second minimum has its origin in the intrinsic asymmetric shape of the AFM skyrmion, with respect to the skyrmion core residing in one of the sublattices, as illustrated in Supplementary Fig. 6. When interfaced with the Fe–FM spins, the Cr spins, residing in the background of sublattice L1, tilt away from their initial direction, while those residing in sublattice L2 get more collinear and antiferromagnetically aligned with respect to the Fe-magnetization, see the red and blue plots respectively in Fig. 5f, obtained along the purple line in Fig. 5a, when positioning the Cr skyrmion at the second minimum. At the vicinity of the Fe–FM skyrmion, the interaction picture gets reversed, which leads to the sublattice-dependent interaction profile shown in Fig. 5e. In particular, the asymmetric profile of the AFM skyrmions, together with the magnetic interaction across the sublattices, enable an energy gain in an area of sublattice L1, where the Cr spins benefit from the AFM coupling with the core of the Fe skyrmion (see the kink in the spin profile highlighted in the inset of Fig. 5f). Unveiling the interaction profile between AFM and FM skyrmions holds significant importance, as it offers an opportunity for manipulating and regulating the trajectories and dynamics of AFM skyrmions by strategically positioning pinned FM skyrmions at the Fe layer.

Discussion

In this study, we uncovered the intricate dynamics of intrinsic AFM skyrmions subjected to perpendicular-to-plane spin-polarized currents, with a particular attention to the impact of FM skyrmions emerging in a hybrid heterostructure (Cr/Pd/Fe/Ir(111) surface) made of an AFM layer (Cr) separated from a FM layer (Fe) by a Pd spacer layer. In contrast to expectations, even for AFM skyrmions, we demonstrate the emergence of the SkHE stemming from the elliptical shape of the topological states. Both the SkHE and skyrmion velocity are anisotropic and follow well-defined dependencies with respect to the polarization direction of the applied currents. The ability to manipulate the polarization direction of spin currents provides a clear avenue for designing tracks where the SkHE either diminishes or persists. However, we would like to emphasize that while we demonstrate the SkHE for elliptical AFM skyrmions in our specific system, our findings extend beyond this particular case. As explained in Supplementary Note 2 and in our previous findings[50], AFM skyrmions formed on triangular lattices hosting a RW-AFM state, tend to exhibit elliptical shapes. Moreover, achieving isotropic shape in these skyrmions requires meeting specific conditions, such as a defined ratio between exchange interaction parameters, the 1st and the 2nd nearest neighbor Heisenberg exchange interactions (J_1 and J_2). Therefore, our results are not confined to a singular system but rather offer insights applicable to a broader class of AFM skyrmions emerging on triangular lattices. Moreover, the presence of non-trivial magnetic states in the FM film can impact the dynamics of the AFM skyrmions by tuning both their velocity and trajectory. For instance, FM skyrmions act as pinning centers, which, depending on the applied current, can deflect AFM skyrmions. The seeding of FM skyrmions modifies the emergent hybrid AFM–FM skyrmionic interaction profile non-trivially. This profile can host several minima, offering the potential of customizing pathways for the motion of AFM skyrmions (see examples illustrated in Supplementary Fig. 7).

In summary, our study advances the understanding of AFM skyrmion dynamics and their interplay with FM skyrmions. These insights hold great promise for the development of innovative spintronic devices that harness the unique properties of AFM and FM spin textures. As the field of AFM spintronics continues to evolve, this research contributes to the foundation

for efficient information processing and storage schemes, potentially revolutionizing the realm of next-generation spintronic technologies.

Methods

To simulate the trilayer of Cr/Pd/Fe, deposited on Ir(111) with fcc stacking, we employ Density functional theory (DFT). To relax the magnetic layers, we use the Quantum-Espresso computational package[86]. The projector augmented wave pseudopotentials from the PS Library[87] and a $28 \times 28 \times 1$ k-point grid were used for the calculations. Then, the electronic structure and magnetic properties were simulated using the all-electron full-potential relativistic Koringa–Kohn–Rostoker (KKR) Green function method[88–90] in the local spin density approximation. The Heisenberg exchange interactions and DMI vectors were extracted using the infinitesimal rotation method[91,92] with a k-mesh of a 200×200. More details on the simulation procedure can be found in ref. 49.

Atomistic spin dynamics

To explore the intricate dynamics of the AFM skyrmions, we conducted atomistic spin simulations. In our study, we consider a two-dimensional Heisenberg model on a triangular lattice, equipped with Heisenberg exchange coupling, DMI, the magnetic anisotropy energy, and the Zeeman term. All parameters were obtained from ab initio. The energy functional reads as follows:

$$\mathcal{H} = \mathcal{H}_{\mathrm{Exc}} + \mathcal{H}_{\mathrm{DMI}} + \mathcal{H}_{\mathrm{Ani}} + \mathcal{H}_{\mathrm{Zeem}}, \tag{5}$$

with:

$$\begin{aligned}
\mathcal{H}_{\mathrm{Exc}} &= -\sum_{<i,j>} J_{ij}^{\mathrm{Cr-Cr}}\, \mathbf{S}_i \cdot \mathbf{S}_j - \sum_{<i,j>} J_{ij}^{\mathrm{Fe-Cr}}\, \mathbf{S}_i \cdot \mathbf{S}_j - \sum_{<i,j>} J_{ij}^{\mathrm{Fe-Fe}}\, \mathbf{S}_i \cdot \mathbf{S}_j, \\
\mathcal{H}_{\mathrm{DMI}} &= \sum_{<i,j>} \mathbf{D}_{ij}^{\mathrm{Cr-Cr}} \cdot [\mathbf{S}_i \times \mathbf{S}_j] + \sum_{<i,j>} \mathbf{D}_{ij}^{\mathrm{Fe-Cr}} \cdot [\mathbf{S}_i \times \mathbf{S}_j] \\
&\quad + \sum_{<i,j>} \mathbf{D}_{ij}^{\mathrm{Fe-Fe}} \cdot [\mathbf{S}_i \times \mathbf{S}_j], \\
\mathcal{H}_{\mathrm{Ani}} &= -K^{\mathrm{Cr}} \sum_i (S_i^z)^2 - K^{\mathrm{Fe}} \sum_i (S_i^z)^2, \\
\mathcal{H}_{\mathrm{Zeem}} &= -\sum_i h_i S_i^z,
\end{aligned}$$

where i and j are site indices carrying each magnetic moments. $\mathbf{S}_i$ is the unit vector of the magnetic moment residing at site i. $J_{ij}^{\mathrm{X-Y}}$ is the Heisenberg exchange coupling strength, being <0 for AFM interaction, between an X atom on site i and a Y atom on site j. A similar notation is adopted for the DMI vector $\mathbf{D}$ and the magnetic anisotropy energy K. The latter favors the out-of-plane orientation of the magnetization. In order to promote the formation of a single AFM skyrmion, independent of the Fe magnetic state's influence; we reduced the Cr atom magnetic anisotropy from 0.5 to 0.4 meV per magnetic atom in this study. The Zeeman coupling, of the atomic spin moment μ_i at site i to an magnetic out-of-plane field, is described by $h_i = \mu_i B$.

Landau–Lifshitz–Gilbert (LLG) equation for CPP

We apply the spin-polarized CPP injection to induce the transitional motion of AFM skyrmions. In the CPP case, the current is perpendicular to the film plane, but polarized in an in-plane direction. The dynamics of the magnetization $\mathbf{S}_i$ at the lattice site i is then governed by the extended LLG equation, which takes the STT terms into account[41,42,74–76],

$$\begin{aligned}
\frac{\mathrm{d}\mathbf{S}_i}{\mathrm{d}t} &= -\frac{\gamma}{(1+\alpha^2)\mu_i}\mathbf{S}_i \times \mathbf{B}_{\mathrm{eff}}^i - \frac{\gamma\alpha}{(1+\alpha^2)\mu_i}\mathbf{S}_i \times \left(\mathbf{S}_i \times \mathbf{B}_{\mathrm{eff}}^i\right) \\
&\quad - \frac{\gamma\alpha\eta}{(1+\alpha^2)\mu_B}\mathbf{S}_i \times \mathbf{S}_p + \frac{\gamma\eta}{(1+\alpha^2)\mu_B}\mathbf{S}_i \times \left(\mathbf{S}_i \times \mathbf{S}_p\right),
\end{aligned} \tag{6}$$

where γ is the gyromagnetic ratio, α is the Gilbert damping parameter, $\mathbf{B}_{\mathrm{eff}}^i \propto -\frac{\partial \mathcal{H}}{\partial \mathbf{S}_i}$ is the effective field, $\mathbf{S}_p$ is the direction of the polarized current and

$$\eta = \frac{j_s P g \mu_B}{2edM_s\gamma}$$

gives the amplitude of the polarized current. The quantities that determine the amplitude are the current density j_s, the polarization P, the saturation magnetization M_s, the Landé factor g, the magnitude of the electron charge e, the Bohr magneton μ_B, the film thickness d, and the gyromagnetic ratio γ. In our study, we utilize the LLG equation as implemented in the Spirit code[93]. We assumed periodic boundary conditions to model the extended two-dimensional system with cells containing 200^2 spins. In our simulations, we used several values of η/α, ranging from 0.001 reaching 0.1 meV, with the in-plane spin polarization direction, $\mathbf{S}_p$, is set at different angles as clarified earlier. All simulations were carried out at zero Kelvin.

Data availability

The data that support the findings of this study are available from the corresponding author upon reasonable request.

Code availability

We used the SPIRIT code, which can be found at https://github.com/spirit-code/spirit. Additionally, the KKR code, a sophisticated ab initio DFT tool, can be found at https://github.com/JuDFTteam/JuKKR.

Received: 20 March 2024; Accepted: 19 July 2024;
Published online: 02 August 2024

References

1. Roessler, U. K., Bogdanov, A. & Pfleiderer, C. Spontaneous skyrmion ground states in magnetic metals. *Nature* **442**, 797–801 (2006).
2. Fert, A., Cros, V. & Sampaio, J. Skyrmions on the track. *Nat. Nanotechnol.* **8**, 152 (2013).
3. Nagaosa, N. & Tokura, Y. Topological properties and dynamics of magnetic skyrmions. *Nat. Nanotechnol.* **8**, 899 (2013).
4. Finocchio, G., Büttner, F., Tomasello, R., Carpentieri, M. & Kläui, M. Magnetic skyrmions: from fundamental to applications. *J. Phys. D Appl.* **49**, 423001 (2016).
5. Fert, A., Reyren, N. & Cros, V. Magnetic skyrmions: advances in physics and potential applications. *Nat. Rev. Mater.* **2**, 17031 (2017).
6. Everschor-Sitte, K., Masell, J., Reeve, R. M. & Kläui, M. Perspective: magnetic skyrmions-overview of recent progress in an active research field. *J. Appl. Phys*. **124**, 240901 (2018).
7. Zhou, Y. Magnetic skyrmions: intriguing physics and new spintronic device concepts. *Natl. Sci. Rev.* **6**, 210–212 (2019).
8. Zhang, X. et al. Skyrmion-electronics: writing, deleting, reading and processing magnetic skyrmions toward spintronic applications. *J. Phys.: Condens. Matter* **32**, 143001 (2020).
9. Zhang, H. et al. Magnetic skyrmions: materials, manipulation, detection, and applications in spintronic devices. *Mater. Futures* **2**, 032201 (2023).
10. Wang, Z.-q. et al. Switching intrinsic magnetic skyrmions with controllable magnetic anisotropy in van der Waals multiferroic heterostructures. *Nano Lett*. **24**, 4117–4123 (2024).
11. Zhang, X., Ezawa, M. & Zhou, Y. Magnetic skyrmion logic gates: conversion, duplication and merging of skyrmions. *Sci. Rep.* **5**, 9400 (2015).
12. Kang, W., Huang, Y., Zhang, X., Zhou, Y. & Zhao, W. Skyrmion-electronics: an overview and outlook. *Proc. IEEE* **104**, 2040–2061 (2016).
13. Prychynenko, D. et al. Magnetic skyrmion as a nonlinear resistive element: a potential building block for reservoir computing. *Phys. Rev. Appl.* **9**, 014034 (2018).

14. Nozaki, T. et al. Brownian motion of skyrmion bubbles and its control by voltage applications. *Appl. Phys. Lett.* **114**, 012402 (2019).
15. Iwasaki, J., Mochizuki, M. & Nagaosa, N. Current-induced skyrmion dynamics in constricted geometries. *Nat. Nanotechnol.* **8**, 742–747 (2013).
16. Zhang, X. et al. Skyrmion-skyrmion and skyrmion-edge repulsions in skyrmion-based racetrack memory. *Sci. Rep.* **5**, 7643 (2015).
17. Bessarab, P. F., Uzdin, V. M. & Jónsson, H. Method for finding mechanism and activation energy of magnetic transitions, applied to skyrmion and antivortex annihilation. *Comput. Phys. Commun.* **196**, 335 (2015).
18. Romming, N. et al. Writing and deleting single magnetic skyrmions. *Science* **341**, 636 (2013).
19. Woo, S. et al. Observation of room-temperature magnetic skyrmions and their current-driven dynamics in ultrathin metallic ferromagnets. *Nat. Mater.* **15**, 501 (2016).
20. Legrand, W. et al. Room-temperature current-induced generation and motion of sub-100 nm skyrmions. *Nano Lett.* **17**, 2703–2712 (2017).
21. Fernandes, I. L., Bouaziz, J., Blügel, S. & Lounis, S. Universality of defect-skyrmion interaction profiles. *Nat. Commun.* **9**, 4395 (2018).
22. Fernandes, I. L., Chico, J. & Lounis, S. Impurity-dependent gyrotropic motion, deflection and pinning of current-driven ultrasmall skyrmions in PdFe/Ir (111) surface. *J. Phys. Condens. Matter* **32**, 425802 (2020).
23. Arjana, I. G., Lima Fernandes, I., Chico, J. & Lounis, S. Sub-nanoscale atom-by-atom crafting of skyrmion-defect interaction profiles. *Sci. Rep.* **10**, 14655 (2020).
24. Jonietz, F. et al. Spin transfer torques in MnSi at ultralow current densities. *Science* **330**, 1648 (2010).
25. Miron, I. M. et al. Fast current-induced domain-wall motion controlled by the Rashba effect. *Nat. Mater.* **10**, 419–423 (2011).
26. Yu, X. et al. Skyrmion flow near room temperature in an ultralow current density. *Nat. Commun.* **3**, 988 (2012).
27. Yang, S.-H., Ryu, K.-S. & Parkin, S. Domain-wall velocities of up to 750 m s- 1 driven by exchange-coupling torque in synthetic antiferromagnets. *Nat. Nanotechnol.* **10**, 221–226 (2015).
28. Sampaio, J., Cros, V., Rohart, S., Thiaville, A. & Fert, A. Nucleation, stability and current-induced motion of isolated magnetic skyrmions in nanostructures. *Nat. Nanotechnol.* **8**, 839 (2013).
29. Zhang, X. et al. All-magnetic control of skyrmions in nanowires by a spin wave. *Nanotechnology* **26**, 225701 (2015).
30. Komineas, S. & Papanicolaou, N. Skyrmion dynamics in chiral ferromagnets. *Phys. Rev. B* **92**, 064412 (2015).
31. Kong, L. & Zang, J. Dynamics of an insulating skyrmion under a temperature gradient. *Phys. Rev. Lett.* **111**, 067203 (2013).
32. Ma, C. et al. Electric field-induced creation and directional motion of domain walls and skyrmion bubbles. *Nano Lett.* **19**, 353–361 (2018).
33. Tomasello, R., Komineas, S., Siracusano, G., Carpentieri, M. & Finocchio, G. Chiral skyrmions in an anisotropy gradient. *Phys. Rev. B* **98**, 024421 (2018).
34. Xia, H. et al. Skyrmion motion driven by the gradient of voltage-controlled magnetic anisotropy. *J. Magn. Magn. Mater.* **458**, 57–61 (2018).
35. Wang, X. et al. Efficient skyrmion transport mediated by a voltage controlled magnetic anisotropy gradient. *Nanoscale* **10**, 733–740 (2018).
36. Yang, Y. et al. Acoustic-driven magnetic skyrmion motion. *Nat. Commun.* **15**, 1018 (2024).
37. Liang, J. et al. Magnetic field gradient driven dynamics of isolated skyrmions and antiskyrmions in frustrated magnets. *New J. Phys.* **20**, 053037 (2018).
38. Cortés-Ortuño, D. et al. Thermal stability and topological protection of skyrmions in nanotracks. *Sci. Rep.* **7**, 4060 (2017).
39. Everschor-Sitte, K. & Sitte, M. Real-space berry phases: skyrmion soccer. *J. Appl. Phys.* **115**, 172602 (2014).
40. Jiang, W. et al. Direct observation of the skyrmion hall effect. *Nat. Phys.* **13**, 162–169 (2017).
41. Zhang, X., Zhou, Y. & Ezawa, M. Antiferromagnetic skyrmion: stability, creation and manipulation. *Sci. Rep.* **6**, 24795 (2016).
42. Zhang, X., Zhou, Y. & Ezawa, M. Magnetic bilayer-skyrmions without skyrmion hall effect. *Nat. Commun.* **7**, 10293 (2016).
43. Barker, J. & Tretiakov, O. A. Static and dynamical properties of antiferromagnetic skyrmions in the presence of applied current and temperature. *Phys. Rev. Lett.* **116**, 147203 (2016).
44. Dohi, T., DuttaGupta, S., Fukami, S. & Ohno, H. Formation and current-induced motion of synthetic antiferromagnetic skyrmion bubbles. *Nat. Commun.* **10**, 5153 (2019).
45. Rosales, H. D., Cabra, D. C. & Pujol, P. Three-sublattice skyrmion crystal in the antiferromagnetic triangular lattice. *Phys. Rev. B* **92**, 214439 (2015).
46. Dos Santos, F. J., dos Santos Dias, M. & Lounis, S. Modeling spin waves in noncollinear antiferromagnets: Spin-flop states, spin spirals, skyrmions, and antiskyrmions. *Phys. Rev. B* **102**, 104436 (2020).
47. Bessarab, P. et al. Stability and lifetime of antiferromagnetic skyrmions. *Phys. Rev. B* **99**, 140411 (2019).
48. Potkina, M. N., Lobanov, I. S., Jónsson, H. & Uzdin, V. M. Skyrmions in antiferromagnets: thermal stability and the effect of external field and impurities. *J. Appl. Phys.* **127**, 213906 (2020).
49. Aldarawsheh, A. et al. Emergence of zero-field non-synthetic single and interchained antiferromagnetic skyrmions in thin films. *Nat. Commun.* **13**, 7369 (2022).
50. Aldarawsheh, A., Sallermann, M., Abusaa, M. & Lounis, S. A spin model for intrinsic antiferromagnetic skyrmions on a triangular lattice. *Front. Phys*. **11**, 1175317 (2023).
51. Velkov, H. et al. Phenomenology of current-induced skyrmion motion in antiferromagnets. *New J. Phys.* **18**, 075016 (2016).
52. Jin, C., Song, C., Wang, J. & Liu, Q. Dynamics of antiferromagnetic skyrmion driven by the spin hall effect. *Appl. Phys. Lett.* **109**, 182404 (2016).
53. Göbel, B., Mook, A., Henk, J. & Mertig, I. Antiferromagnetic skyrmion crystals: generation, topological hall, and topological spin hall effect. *Phys. Rev. B* **96**, 060406 (2017).
54. Akosa, C. A., Tretiakov, O., Tatara, G. & Manchon, A. Theory of the topological spin hall effect in antiferromagnetic skyrmions: impact on current-induced motion. *Phys. Rev. Lett.* **121**, 097204 (2018).
55. Legrand, W. et al. Room-temperature stabilization of antiferromagnetic skyrmions in synthetic antiferromagnets. *Nat. Mater.* **19**, 34 (2020).
56. Finco, A. et al. Imaging non-collinear antiferromagnetic textures via single spin relaxometry. *Nat. Commun.* **12**, 767 (2021).
57. Juge, R. et al. Skyrmions in synthetic antiferromagnets and their nucleation via electrical current and ultra-fast laser illumination. *Nat. Commun.* **13**, 4807 (2022).
58. Chen, R. et al. Controllable generation of antiferromagnetic skyrmions in synthetic antiferromagnets with thermal effect. *Adv. Funct. Mater.* **32**, 2111906 (2022).
59. Pham, V. T. et al. Fast current-induced skyrmion motion in synthetic antiferromagnets. *Science* **384**, 307–312 (2024).
60. Chmiel, F. P. et al. Observation of magnetic vortex pairs at room temperature in a planar α-Fe_2O_3/Co heterostructure. *Nat. Mater.* **17**, 581–585 (2018).
61. Gao, S. et al. Fractional antiferromagnetic skyrmion lattice induced by anisotropic couplings. *Nature* **586**, 37 (2020).
62. Jani, H. et al. Antiferromagnetic half-skyrmions and bimerons at room temperature. *Nature* **590**, 74 (2021).
63. Aldarawsheh, A., Sallermann, M., Abusaa, M. & Lounis, S. Intrinsic Néel antiferromagnetic multimeronic spin textures in ultrathin films. *The J. Phys. Chem. Lett. Chemistry Letters* **14**, 8970–8978 (2023).

64. Dupé, B., Hoffmann, M., Paillard, C. & Heinze, S. Tailoring magnetic skyrmions in ultra-thin transition metal films. *Nat. Commun.* **5**, 4030 (2014).
65. Simon, E., Palotás, K., Rózsa, L., Udvardi, L. & Szunyogh, L. Formation of magnetic skyrmions with tunable properties in PdFe bilayer deposited on Ir (111). *Phys. Rev. B* **90**, 094410 (2014).
66. Romming, N., Kubetzka, A., Hanneken, C., von Bergmann, K. & Wiesendanger, R. Field-dependent size and shape of single magnetic skyrmions. *Phys. Rev. Lett.* **114**, 177203 (2015).
67. Crum, D. M. et al. Perpendicular reading of single confined magnetic skyrmions. *Nat. Commun.* **6**, 8541 (2015).
68. Fernandes, I. L., Bouhassoune, M. & Lounis, S. Defect-implantation for the all-electrical detection of non-collinear spin-textures. *Nat. Commun.* **11**, 1602 (2020).
69. Bouhassoune, M. & Lounis, S. Friedel oscillations induced by magnetic skyrmions: from scattering properties to all-electrical detection. *Nanomaterials* **11**, 194 (2021).
70. Lima Fernandes, I., Blügel, S. & Lounis, S. Spin-orbit enabled all-electrical readout of chiral spin-textures. *Nat. Commun.* **13**, 1576 (2022).
71. Spethmann, J. et al. Discovery of magnetic single-and triple-q states in Mn/Re (0001). *Phys. Rev. Lett.* **124**, 227203 (2020).
72. Spethmann, J., Grünebohm, M., Wiesendanger, R., von Bergmann, K. & Kubetzka, A. Discovery and characterization of a new type of domain wall in a row-wise antiferromagnet. *Nat. Commun.* **12**, 3488 (2021).
73. Kurz, P. *Non-collinear Magnetism at Surfaces and in Ultrathin Films*. Ph.D. thesis, Elektronische Eigenschaften (2001).
74. Slonczewski, J. Current-driven excitation of magnetic multilayers. *J. Magn. Magn. Mater.* **159**, L1–L7 (1996).
75. Chureemart, P., Evans, R. & Chantrell, R. Dynamics of domain wall driven by spin-transfer torque. *Phys. Rev. B* **83**, 184416 (2011).
76. Schürhoff, D. C. B. *Atomistic Spin Dynamics with Real Time Control of Simulation Parameters and Visualisation*. Master Thesis, RWTH Aachen (2016).
77. Xia, J. et al. Current-driven dynamics of frustrated skyrmions in a synthetic antiferromagnetic bilayer. *Phys. Rev. Appl.* **11**, 044046 (2019).
78. Lee, S.-J., Kim, K.-W., Lee, H.-W. & Lee, K.-J. Spin-orbit-torque-induced skyrmion dynamics for different types of spin-orbit coupling. *J. Magn. Magn. Mater.* **455**, 14–18 (2018).
79. Thiele, A. Steady-state motion of magnetic domains. *Phys. Rev. Lett.* **30**, 230 (1973).
80. Kim, S. K., Lee, K.-J. & Tserkovnyak, Y. Self-focusing skyrmion racetracks in ferrimagnets. *Phys. Rev. B* **95**, 140404 (2017).
81. Panigrahy, S., Mallick, S., Sampaio, J. & Rohart, S. Skyrmion inertia in synthetic antiferromagnets. *Phys. Rev. B* **106**, 144405 (2022).
82. Zhang, X., Ezawa, M. & Zhou, Y. Thermally stable magnetic skyrmions in multilayer synthetic antiferromagnetic racetracks. *Phys. Rev. B* **94**, 064406 (2016).
83. Xia, J. et al. Dynamics of an elliptical ferromagnetic skyrmion driven by the spin–orbit torque. *Appl. Phys. Lett*. **116**, 022407 (2020).
84. Huang, S. et al. Stabilization and current-induced motion of antiskyrmion in the presence of anisotropic Dzyaloshinskii-Moriya interaction. *Phys. Rev. B* **96**, 144412 (2017).
85. Chen, J. et al. Dynamics of distorted skyrmions in strained chiral magnets. *New J. Phys.* **20**, 063050 (2018).
86. Giannozzi, P. et al. Quantum espresso: a modular and open-source software project for quantum simulations of materials. *J. Phys. Condens. Matter* **21**, 395502 (2009).
87. Dal Corso, A. Pseudopotentials periodic table: from *H* to *Pu*. *Comput. Mater. Sci.* **95**, 337–350 (2014).
88. Papanikolaou, N., Zeller, R. & Dederichs, P. H. Conceptual improvements of the KKR method. *J. Phys. Condens. Matter* **14**, 2799 (2002).
89. Bauer, D. S. G. *Development of A Relativistic Full-potential First-principles Multiple Scattering Green Function Method Applied to Complex Magnetic Textures of Nano Structures at Surfaces*. PhD Thesis, RWTH Aachen (2014).
90. Rüßmann, P. & JuDFTteam. JuDFTteam/JuKKR: v3.6. *Zenodo* https://doi.org/10.5281/zenodo.7284739 (2022).
91. Liechtenstein, A., Katsnelson, M., Antropov, V. & Gubanov, V. Local spin density functional approach to the theory of exchange interactions in ferromagnetic metals and alloys. *J. Magn. Magn. Mater.* **67**, 65–74 (1987).
92. Ebert, H. & Mankovsky, S. Anisotropic exchange coupling in diluted magnetic semiconductors: *ab initio* spin-density functional theory. *Phys. Rev. B* **79**, 045209 (2009).
93. Müller, G. P. et al. Spirit: Multifunctional framework for atomistic spin simulations. *Phys. Rev. B* **99**, 224414 (2019).

Acknowledgements

This work was supported by the Federal Ministry of Education and Research of Germany in the framework of the Palestinian-German Science Bridge (BMBF grant number 01DH16027) and the Deutsche Forschungsgemeinschaft (DFG) through SPP 2137 “Skyrmionics” (Projects LO 1659/8-1). The authors gratefully acknowledge the computing time granted through JARA on the supercomputer JURECA at Forschungszentrum Jülich. M.S. acknowledges the fund from the European Research Council (ERC) under the European Union’s Horizon 2020 research and innovation program (Grant No. 856538, project “3D MAGiC”.

Author contributions

S.L. initiated, supervised the project. A.A. performed the simulations and analyzed the results with the supervision of S.L. All authors discussed the results. A.A. and S.L. wrote the manuscript to which all co-authors contributed.

Funding

Open Access funding enabled and organized by Projekt DEAL.

Competing interests

The authors declare no competing interests.

Additional information

Supplementary information The online version contains supplementary material available at https://doi.org/10.1038/s44306-024-00049-w.

Correspondence and requests for materials should be addressed to Amal Aldarawsheh or Samir Lounis.